eLIFE
elifesciences.org

Figures and figure supplements

Graded Ca^{2+}/calmodulin-dependent coupling of voltage-gated $Ca_V1.2$ channels

Rose E Dixon, et al.

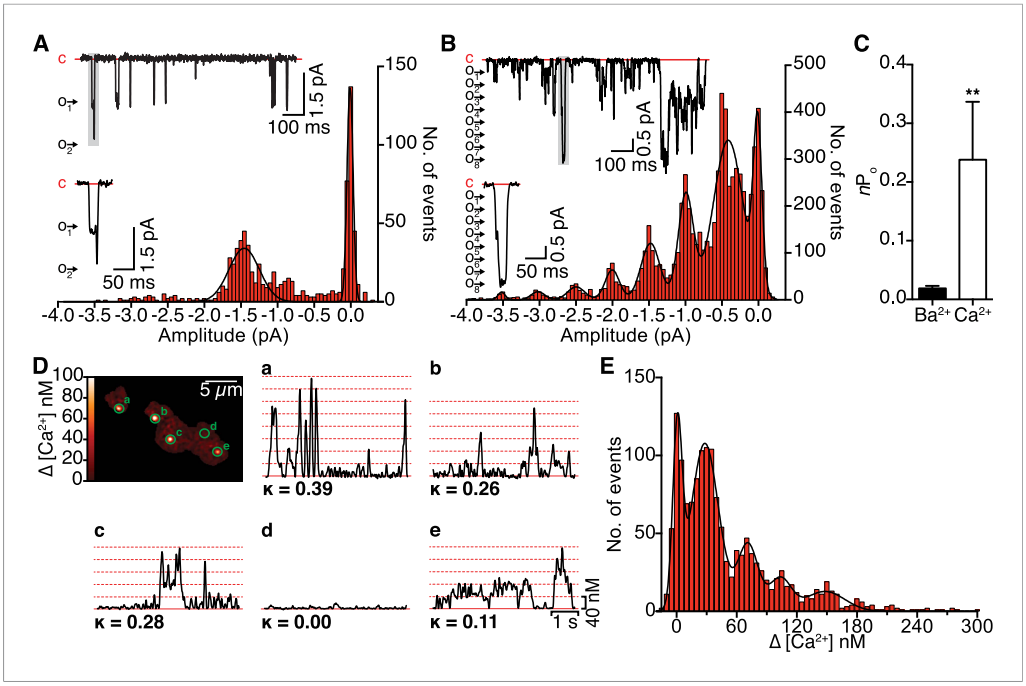

Figure 1. Single-channel electrical and optical recordings of $Ca_v1.2$ channel coupling. (**A** and **B**) Representative i_{Ba} (**A**) and i_{Ca} (**B**) traces and their κ values, recorded from $Ca_v1.2$-expressing tsA-201 cells during step depolarizations from −80 to −30 mV. Amplitude histograms (constructed from $n = 6$ cells each) were fit with multi-component Gaussian functions (solid black lines). A portion of each trace (gray box) is shown enlarged below, showing that the resulting L-type Ca^{2+} current reflects the simultaneous opening and closing of multiple channels with Ca^{2+} as the charge carrier, but not with Ba^{2+} as the charge carrier. (**C**) Bar chart of i_{Ba} and i_{Ca} single-channel activity (nP_o). Data are presented as means ± SEM (**p < 0.01). (**D**) Calibrated TIRF image of an adult ventricular myocyte dialyzed with the Ca^{2+} indicator dye Rhod-2 via the patch pipette (see also ***Video 1***). Time courses of $[Ca^{2+}]_i$ from each sparklet site (indicated by green circles on TIRF image) and their κ values are shown in panels **A**–**E**. (**E**) All-points histogram of Ca^{2+} sparklet data recorded from adult ventricular myocytes. The data were fit with a multi-component Gaussian function (solid black line).

DOI: 10.7554/eLife.05608.003

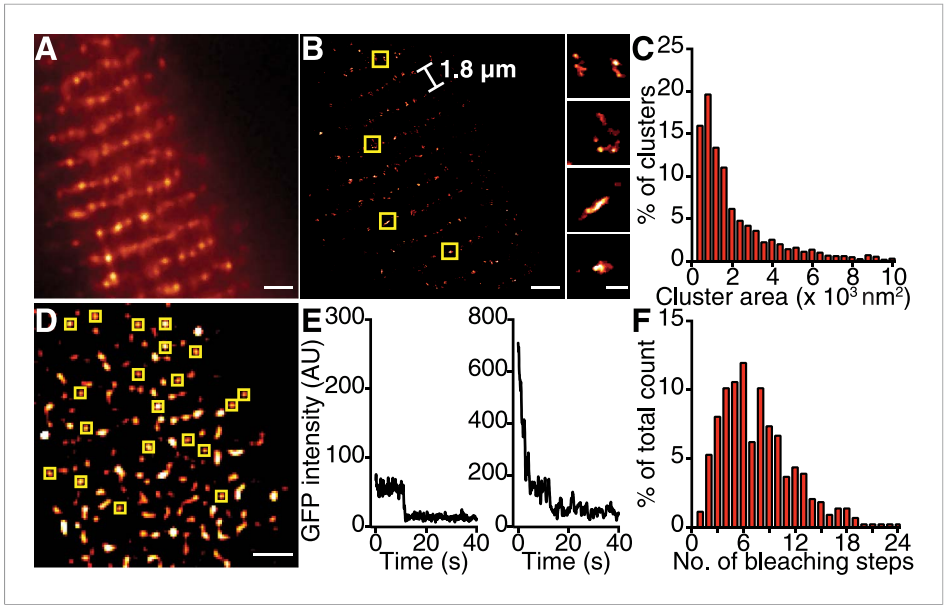

Figure 2. $Ca_v1.2$ channels form clusters in the ventricular myocyte PM. (**A**) TIRF image of a fixed, adult mouse ventricular myocyte immunolabeled with an antibody specific for $Ca_v1.2$ channels. (**B**) Super-resolution GSD image of the same cell. Channels are located along the t-tubule network with the characteristic 1.8-µm separation. Yellow boxes denote location of higher-magnification images of channel clusters (*right*). (**C**) Distribution of cluster areas in ventricular myocytes (n = 5 myocytes). (**D**) An average of the first five frames of a TIRF image time series taken of a myocyte isolated from mice expressing $Ca_v\beta_{2a}$-PA-GFP. Yellow boxes indicate spots selected for analysis. Scale bars = 2 µm. (**E**) Examples of bleaching steps for $Ca_v\beta_{2a}$-PA-GFP associated with $Ca_v1.2$ channels. (**F**) Distribution of bleaching steps obtained from 435 spots selected from n = 11 cells.

DOI: 10.7554/eLife.05608.005

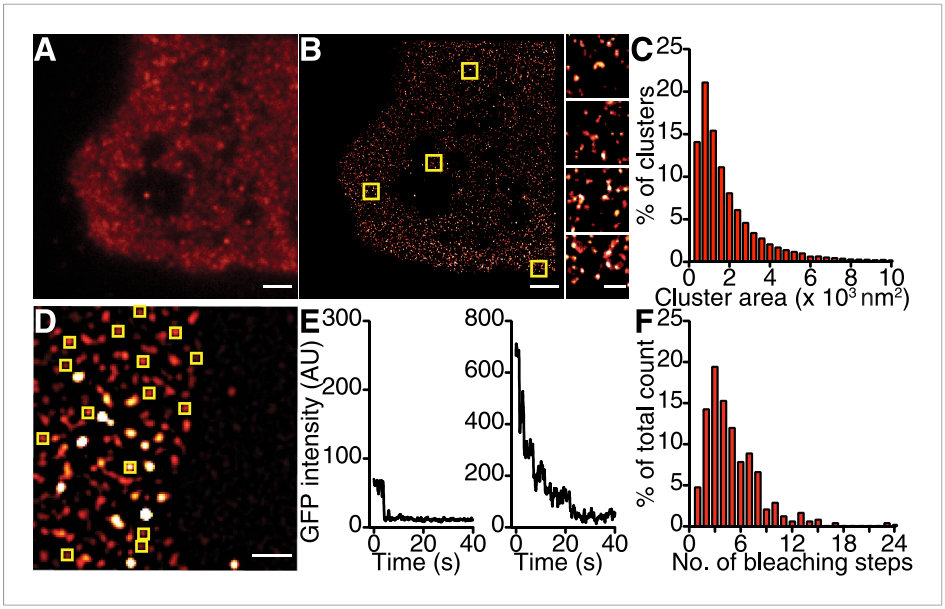

Figure 3. $Ca_v1.2$ channels form clusters in tsA-201 cell membranes. (**A** and **B**) TIRF and GSD images of immunolabeled $Ca_v1.2$ channels in a transfected tsA-201 cell (**A**). Yellow boxes in (**B**) indicate the location of each higher-magnification image (*right*). (**C**) Distribution of cluster areas in tsA-201 cells ($n = 9$ cells). (**D**) An average of the first five frames of a TIRF image time series for a tsA-201 cell expressing $Ca_v1.2$-EGFP. (**E**) Examples of bleaching steps for $Ca_v1.2$-EGFP. Scale bars = 2 μm. (**F**) Distribution of bleaching steps obtained from 484 spots selected from $n = 10$ cells.

DOI: 10.7554/eLife.05608.006

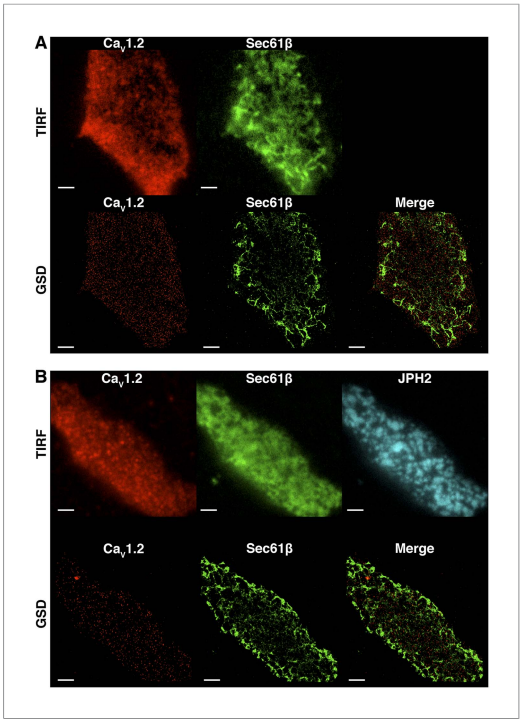

Figure 3—figure supplement 1. $Ca_V1.2$ channel clusters are not co-localized to tsA-201 ER structures. (**A**) TIRF (*top*) and GSD (*bottom*) images of immunolabeled $Ca_V1.2$ channels (*left*) and mCherry-Sec61β (*middle*) in a transfected tsA-201 cell. The image on the bottom right was generated by merging $Ca_V1.2$ and mCherry-Sec61β GSD images. (**B**) *Top*: TIRF images of immunolabeled $Ca_V1.2$ channels (*left*), mCherry-Sec61β (*middle*), and JPH2 (*right*) in a transfected tsA-201 cell. *Bottom*: GSD images from the same cell showing $Ca_V1.2$ channels (*left*), mCherry-Sec61β (*middle*), and a merge of the two (*right*). Scale bars = 2 μm.

DOI: 10.7554/eLife.05608.007

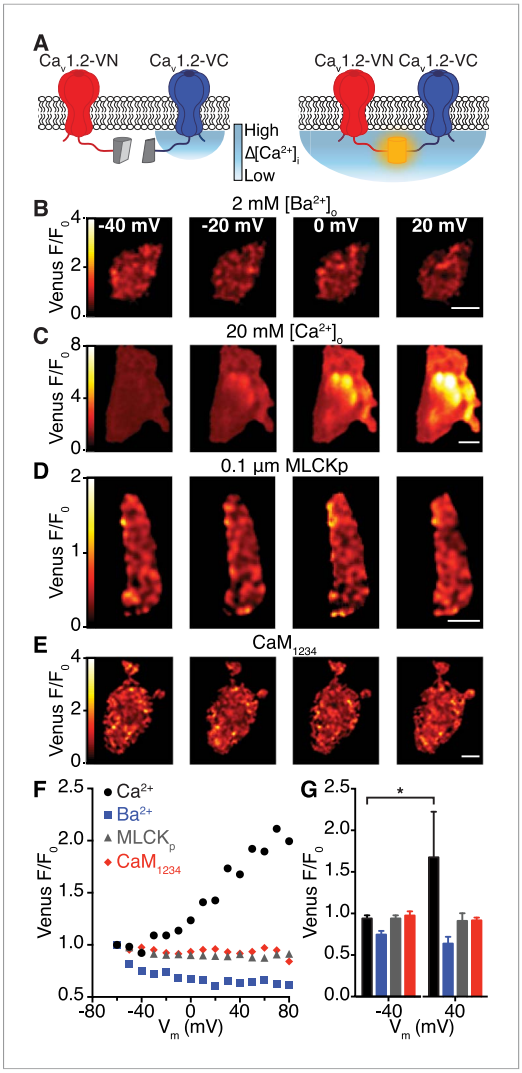

Figure 4. Interactions between $Ca_v1.2$ channel C-termini occur spontaneously and in a Ca^{2+}/CaM-dependent manner. (**A**) Illustration of the bimolecular fluorescence complementation strategy for assaying interactions between $Ca_v1.2$ channel C-termini. Non-interacting channels tagged at their C-terminus with either the N- or C-terminal half of split Venus are non-fluorescent (*left*). Spontaneous interactions between channel C-termini result in reconstitution of Venus and emission of fluorescence (*right*). (**B**–**E**) TIRF images obtained from whole-cell patch-clamped tsA-201 cells expressing $Ca_v1.2$-VN and $Ca_v1.2$-VC over 9-s voltage steps to the indicated potentials. Images were median-filtered, smoothed, pseudo-colored with a 'red-hot' LUT, and divided by the initial –60 mV image to obtain calibrated Venus F/F_0. Experiments were performed with 2 mM Ba^{2+} (**B**) or 20 mM Ca^{2+} (**C**–**E**) in the perfusing solution. Scale bars = 3 µm. (See also ***Figure 4—figure supplement 2***) (**D**) Images obtained during dialysis with MLCKp (0.1 µM). (**E**) Images from a cell in which CaM_{1234} was co-expressed with $Ca_v1.2$-VN and $Ca_v1.2$-VC (see also ***Figure 4—figure supplement 3***). (**F**) Relationship

Figure 4. continued on next page

Figure 4. Continued

between membrane voltage and Venus reconstitution for each experimental condition. (**G**) Bar chart showing mean Venus fluorescence (F/F_0) ± SEM for each condition at −40 and +40 mV (*$p < 0.05$).

DOI: 10.7554/eLife.05608.008

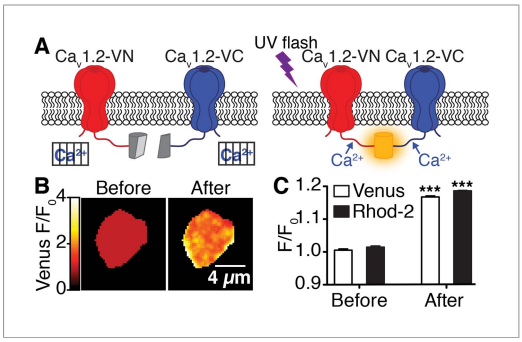

Figure 4—figure supplement 1. Flash photolysis of caged Ca^{2+} stimulates $Ca_v1.2$ interactions. (**A**) Illustration of flash photolysis-induced bimolecular fluorescence complementation. Prior to uncaging of Ca^{2+}, cells were bathed in a zero Ca^{2+} solution; under these conditions, split-Venus–tagged channels do not interact (*left*). Upon application of a UV flash to uncage Ca^{2+}, interactions between the channel C-termini results in reconstitution of Venus protein and emission of fluorescence (*right*). (**B**) Confocal images of Venus fluorescence emission (F/F_0) before and after flash photolysis of caged Ca^{2+}. (**C**) The bar chart shows mean Venus and Rhod-2 fluorescence emission (F/F_0) ± SEM before and after Ca^{2+} uncaging (***$p < 0.001$, for comparison of $Ca_v1.2$ interactions [Venus reconstitution] and intracellular Ca^{2+} concentration [Rhod-2 emission] before and after flash photolysis of caged Ca^{2+}; paired *t*-test).

DOI: 10.7554/eLife.05608.009

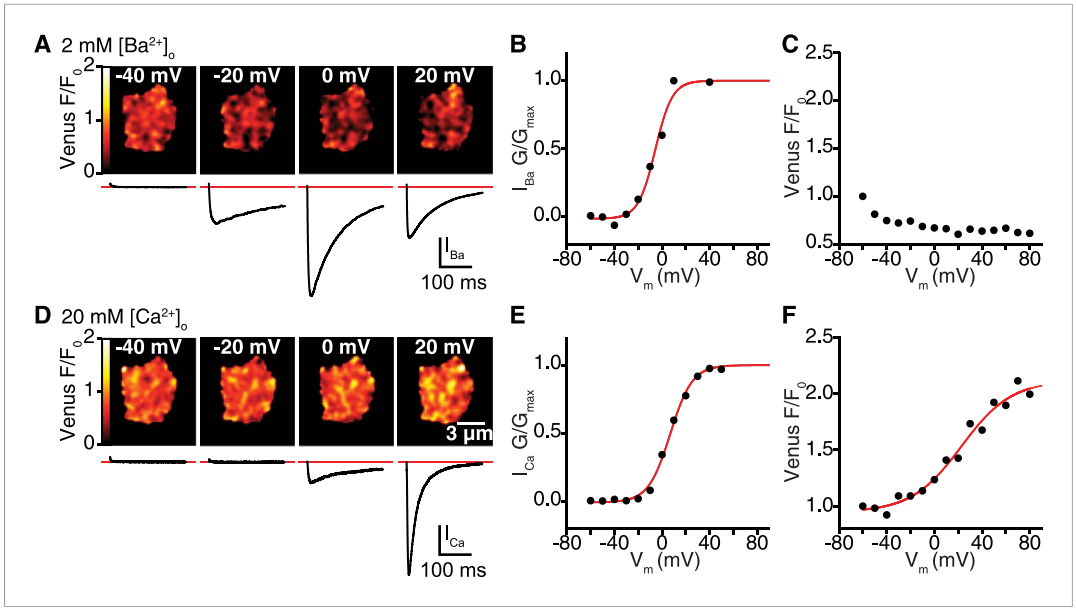

Figure 4—figure supplement 2. $Ca_v1.2$ interactions are Ca^{2+} dependent. (**A**–**C**) Venus fluorescence and $Ca_v1.2$ currents were recorded in whole-cell mode from tsA-201 cells expressing $Ca_v1.2$-VN and $Ca_v1.2$-VC during depolarizing voltage steps to −40, −20, 0 and +20 mV with Ba^{2+} as the charge carrier (2 mM $[Ba^{2+}]_o$). Voltage dependencies were fit with a Boltzmann sigmoidal function (red solid line) except in (**C**), where Venus F/F_0 decayed exponentially during the voltage protocol in a manner reminiscent of photobleaching. (**A**) Calibrated Venus F/F_0 TIRF images (*top*) and I_{Ba} (*bottom*) from a representative tsA-201 cell. (**B**) Voltage dependence of normalized conductance. (**C**) Venus fluorescence (F/F_0) plots. (**D**–**F**) Venus fluorescence and $Ca_v1.2$ currents were recorded as above (**A**–**C**) with Ca^{2+} as the charge carrier (20 mM $[Ca^{2+}]_o$). (**D**) Calibrated Venus F/F_0 TIRF images (*top*) and I_{Ba} (*bottom*) from a representative tsA-201 cell. (**E**)Voltage dependence of normalized conductance. (**F**) Venus fluorescence (F/F_0) plots. Voltage dependencies were fit with a Boltzmann sigmoidal function (red solid line).

DOI: 10.7554/eLife.05608.010

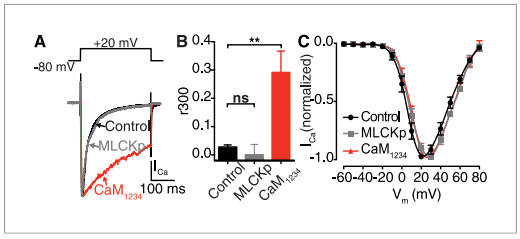

Figure 4—figure supplement 3. Ca^{2+} binding to distinct CaM pools regulates CDI. (**A**–**C**) tsA-201 cells expressing $Ca_v1.2$ were subjected to a 300-ms depolarization from a holding potential of −80 mV to a test potential of +20 mV in the presence of 20 mM $[Ca^{2+}]_o$. (**A**) I_{Ca} elicited under control conditions (20 mM $[Ca^{2+}]_o$), with 0.1 µM MLCKp dialyzed via the patch pipette, and in cells co-expressing Ca^{2+}-insensitive CaM_{1234}. (**B**) Mean r_{300} ratios ± SEM (**p = 0.002). (**C**) Current-voltage relationships.

DOI: 10.7554/eLife.05608.011

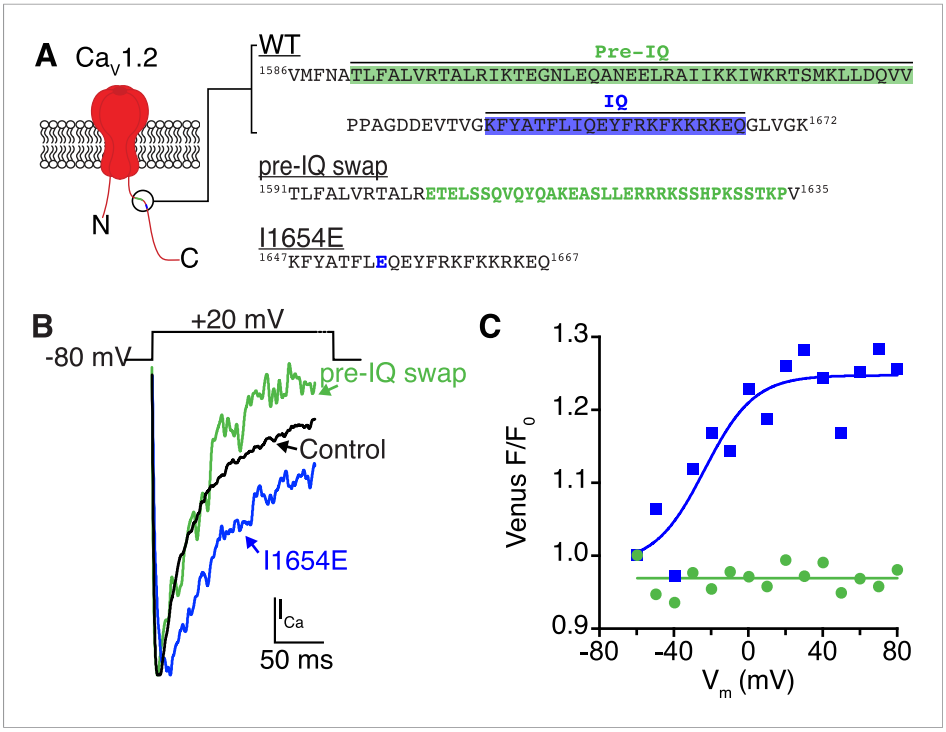

Figure 4—figure supplement 4. Ca^{2+}/CaM binding to the pre-IQ domain, and not the IQ domain, mediates channel coupling. (**A**) Illustration of the pore-forming subunit of a $Ca_V1.2$ channel embedded in the PM, with intracellular N and C-termini. The C-terminus contains pre-IQ (*green*) and IQ (*blue*) motifs, which are known to bind CaM. The amino acid sequence of the pre-IQ and IQ segments of the C-terminus of WT, pre-IQ swap, and I1654E mutant channels used in this study are shown on the *right*. For the pre-IQ swap, a 33-amino-acid segment was replaced with 33 non-identical amino acids. For the I1654E mutation, a point mutation was made replacing I1654 with E. (**B**) I_{Ca} elicited by a depolarizing step from −80 mV to a test potential of +20 mV under control conditions (20 mM $[Ca^{2+}]_o$) in tsA-201 cells expressing WT (*black*), I1624E (*blue*), or pre-IQ swap (*green*) $Ca_V1.2$ channels. (**C**) Venus fluorescence (F/F_0) plots for the two mutant channels. $Ca_V1.2$(I1624E) channels exhibited a voltage-dependent increase in Venus reconstitution that fit a Boltzmann sigmoidal function (blue solid line; $n = 5$). Venus F/F_0 decayed over the course of the voltage protocol in cells expressing $Ca_V1.2$(pre-IQ swap) ($n = 8$).

DOI: 10.7554/eLife.05608.012

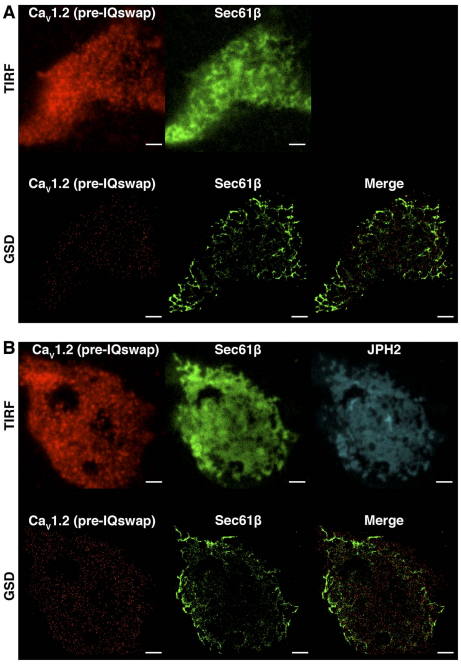

Figure 4—figure supplement 5. $Ca_V1.2$ channel clustering is necessary but not sufficient for functional coupling. (**A**) TIRF (*top*) and super-resolution GSD (*bottom*) images of immunolabeled $Ca_V1.2$(pre-IQ swap) channels (*left*) and mCherry-Sec61β (*middle*) in an exemplary transfected tsA-201 cell. The image on the bottom right was generated by merging $Ca_V1.2$(pre-IQ swap) and mCherry-Sec61β GSD images. (**B**) *Top*: TIRF images of immunolabeled $Ca_V1.2$(pre-IQ swap) channels (*left*), mCherry-Sec61β (*middle*), and JPH2-GFP (*right*) in a transfected tsA-201 cell. *Bottom*: GSD images from the same cell showing $Ca_V1.2$(pre-IQ swap) channels (*left*), mCherry-Sec61β (*middle*), and a merge of the two (*right*). Scale bars = 2 μm.

DOI: 10.7554/eLife.05608.013

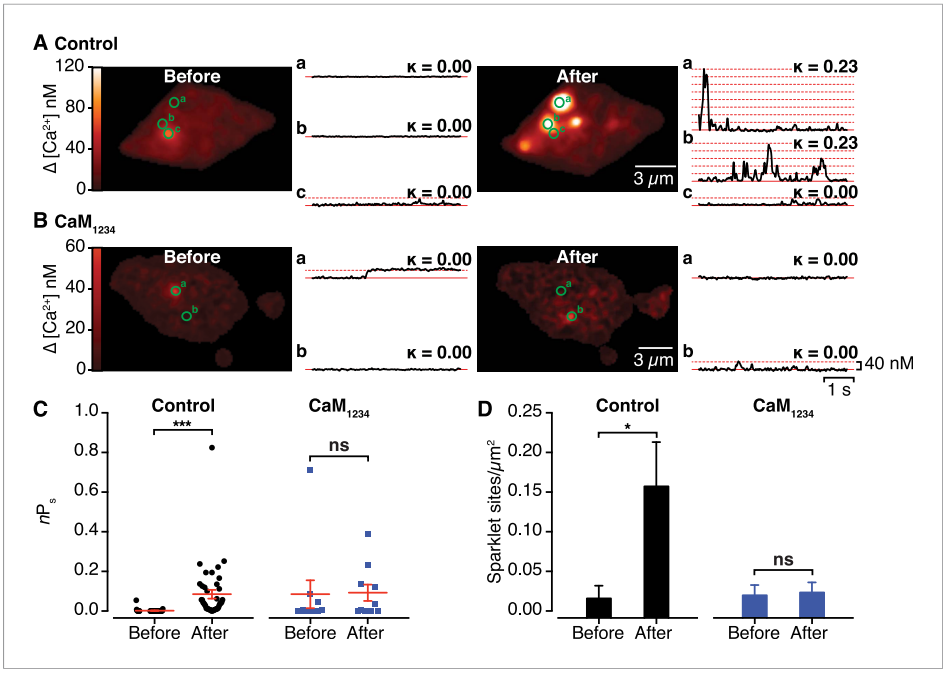

Figure 5. Effects of interactions between $Ca_v1.2$ channel C-termini on channel activity. (**A** and **B**) Calibrated TIRF images (see also ***Video 2***) of representative control tsA-201 cells (**A**) and tsA-201 cells expressing the Ca^{2+}-insensitive CaM_{1234} mutant (**B**). In both cases, cells expressed $Ca_v1.2$-VN and $Ca_v1.2$-VC and were loaded with Rhod-2 via the patch pipette. Cells were held at −80 mV during sparklet recordings before (*left*) and after (*right*) depolarization to +60 mV. The time course of $[Ca^{2+}]_i$ for each sparklet site (denoted by green circles) before and after depolarization is shown to the right of each image. (**C** and **D**) Scatter plots of sparklet activity (**C**; nP_s; ***$p < 0.001$) and sparklet site density (**D**; *$p = 0.03$), before and after depolarization in control ($n = 5$) and CaM_{1234}-expressing ($n = 6$) cells. ns, not significant.

DOI: 10.7554/eLife.05608.014

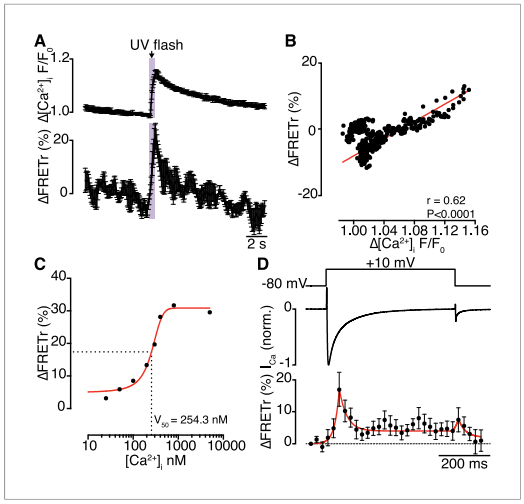

Figure 6. Interactions of $Ca_v1.2$ C-termini occur dynamically with Ca^{2+} influx and are transiently persistent. (**A**) Time course of the percent change in FRETr (*bottom*) evoked by flash photolysis of caged Ca^{2+} (purple box). Experiments were performed at a holding potential of −80 mV with zero EGTA or BAPTA; thus, the change in $[Ca^{2+}]_i$ (F/F_0; *top*) was global. Averaged traces (n = 5 cells) and error bars showing SEM at each sampling point. (**B**) Correlation between changes in FRETr and global $[Ca^{2+}]_i$ produced by caged Ca^{2+} photolysis, showing that increases in $[Ca^{2+}]_i$ were accompanied by an increase in FRETr ($p < 0.0001$). (**C**) Plot of the percent change in FRETr vs $[Ca^{2+}]_i$ (nM). Data (n = 8 cells) were fit to a Boltzmann Sigmoidal function (solid red line) with V_{50} = 254.3 nM (black dashed line). (**D**) Step depolarization (*top*) in the presence of 10 mM EGTA produced local $[Ca^{2+}]_i$ elevation and inactivating I_{Ca} (*middle*). Increased channel interactions, represented as the percent change in FRETr (*bottom;* averaged from n = 6 cells), were detected at the onset of depolarization and repolarization during the peak and tail currents. Dashed line shows FRETr baseline level.

DOI: 10.7554/eLife.05608.016

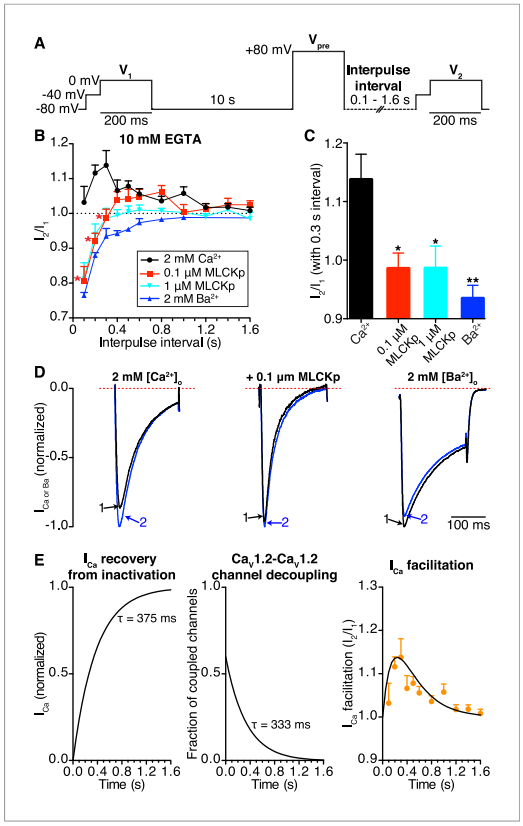

Figure 7. $Ca_V1.2$-to-$Ca_V1.2$ channel coupling is critical for I_{Ca} facilitation in cardiomyocytes. (**A**) Voltage protocol used to evoke I_1 and I_2 in ventricular myocytes. (**B**) Line chart summarizing the current amplitude ratio (I_2/I_1) at 0 mV for each condition over the range of interpulse intervals from 0.1 to 1.6 s. (**C**) Bar chart summarizing the current-amplitude ratio (I_2/I_1) with a fixed interpulse interval of 300 ms for each condition. (**D**) Normalized whole-cell currents evoked by the protocol in (**A**), with 2 mM $[Ca^{2+}]_o$ as the charge carrier without (*left*) or with (*middle*) intracellular dialysis of 0.1 µM MLCKp (*middle*). The currents on the right were recorded with 2 mM $[Ba^{2+}]_o$ as the charge carrier. Data are shown as means + SEM (*$p < 0.05$, **$p < 0.01$ vs control (2 mM $[Ca^{2+}]_o$)). (**E**) Simulated time-course of I_{Ca} recovery from inactivation (*left*), $Ca_V1.2$-$Ca_V1.2$ channel cluster disassembly (*middle*), and I_{Ca} facilitation (solid black line; *right*). Recovery and channel decoupling curves are single exponential functions with time constants (τ) of 375 ms and 333 ms, respectively. The I_{Ca} facilitation curve is the product of the recovery and decoupling functions. For comparison, the experimental facilitation data (orange circles) collected with 2 mM $[Ca^{2+}]_o$ as the charge carrier is plotted alongside the simulated I_{Ca} facilitation data. The amplitude of the decoupling function was scaled to fit the facilitation data.

DOI: 10.7554/eLife.05608.017

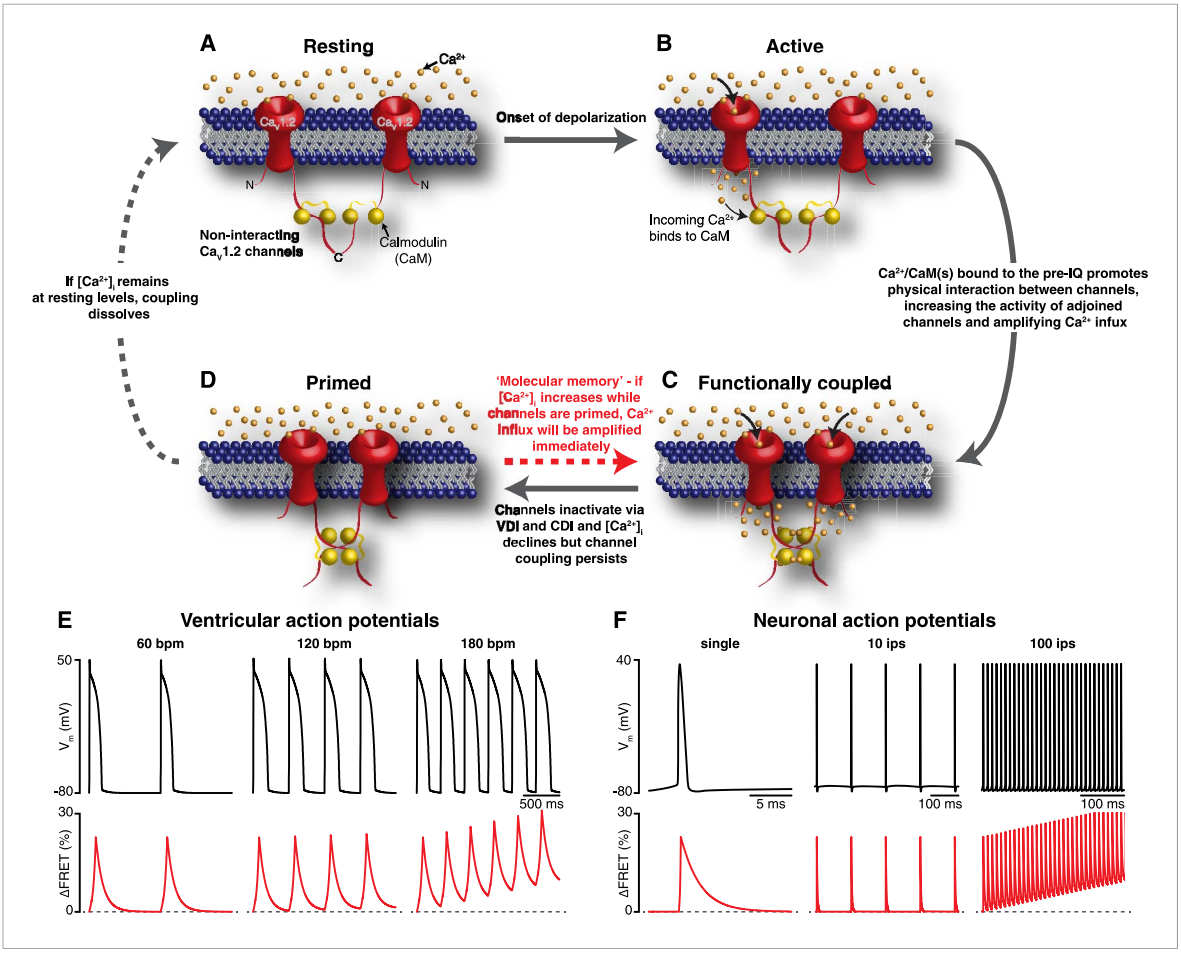

Figure 8. Mechanism and proposed model for the functional coupling of $Ca_V1.2$ channels. (**A**) $Ca_V1.2$ channels are arranged into clusters in the PM of excitable cells; for simplicity, a cluster of two channels is shown. At the resting membrane potential (e.g., –80 mV), $[Ca^{2+}]_i$ and $Ca_V1.2$ P_o are low; hence, the majority of $Ca_V1.2$ channels are non-interacting. (**B**) During an action potential, the PM becomes depolarized, increasing the P_o of independently gating $Ca_V1.2$ channels. Ca^{2+} flows into the cell through these active channels, producing an elevation in local $[Ca^{2+}]_i$ and increasing Ca^{2+} binding to CaM. (**C**) Ca^{2+}/CaM binding to the C-terminal pre-IQ domain of the $Ca_V1.2$ channel promotes physical interactions between adjacent channels. This functional coupling increases the activity of adjoined channels and thus amplifies Ca^{2+} influx. (**D**) $Ca_V1.2$ channels undergo VDI and CDI, and $[Ca^{2+}]_i$ declines once more. However, the channels remain coupled in a 'primed', non-conducting state for a finite time. If the membrane is depolarized again when the channels are still primed, the amplification of Ca^{2+} influx will be immediate; otherwise, if $[Ca^{2+}]_i$ remains at resting levels beyond the lifetime of the primed state, the coupling dissolves and the cycle begins again. (**E**) and (**F**) show proposed rate-dependent changes in $Ca_V1.2$ channel coupling in ventricular myocytes and neurons, respectively. *Top*: Simulated ventricular and neuronal action potentials are depicted at low, intermediate, and high firing rates. *Bottom*: The accompanying dynamic change in $Ca_V1.2$ channel coupling (reflected by FRET changes between adjacent channels). bpm, beats per minute; ips, impulses per second.

DOI: 10.7554/eLife.05608.018